SUPERCONDUCTORS

10.1126/sciadv.1501119

Block copolymer self-assembly–directed synthesis of mesoporous gyroidal superconductors

Spencer W. Robbins,[1,2]* Peter A. Beaucage,[1]* Hiroaki Sai,[1†] Kwan Wee Tan,[1‡] Jörg G. Werner,[1,2] James P. Sethna,[3] Francis J. DiSalvo,[2] Sol M. Gruner,[3,4,5] Robert B. Van Dover,[1] Ulrich Wiesner[1§]

Superconductors with periodically ordered mesoporous structures are expected to have properties very different from those of their bulk counterparts. Systematic studies of such phenomena to date are sparse, however, because of a lack of versatile synthetic approaches to such materials. We demonstrate the formation of three-dimensionally continuous gyroidal mesoporous niobium nitride (NbN) superconductors from chiral ABC triblock terpolymer self-assembly–directed sol-gel–derived niobium oxide with subsequent thermal processing in air and ammonia gas. Superconducting materials exhibit a critical temperature (T_c) of about 7 to 8 K, a flux exclusion of about 5% compared to a dense NbN solid, and an estimated critical current density (J_c) of 440 A cm^{-2} at 100 Oe and 2.5 K. We expect block copolymer self-assembly–directed mesoporous superconductors to provide interesting subjects for mesostructure-superconductivity correlation studies.

INTRODUCTION

Mesoscale structures in the form of periodically ordered mesoporous arrays with pore sizes between 2 and 50 nm and various achiral or chiral mesoscale morphologies are expected to affect the properties of superconductors, including their critical field, critical current, and flux pinning behavior (*1*–*6*). Despite a growing interest in mesoscale science (*7*), only a few studies to date have pursued these phenomena. For example, there have been reports of a superconducting oxide asymmetric membrane with a mesoporous layer on a macroporous substrate (*8*), a sputtered superconducting Nb layer on a nanoporous Si substrate (*9*), lithographically fabricated Nb-shifted strip arrays (*10*), and biotemplated oxide superconductors with micrometer-scale structural ordering (*11*). The sparsity of such studies is attributable, in part, to a lack of synthetic approaches to mesostructured superconductors that allow systematic investigations of the effects of mesostructure on superconductivity. In all of these cases, the materials in question were prepared by lithographic or templating approaches—not self-assembly—and, as a result, offer limited tunability and no access to three-dimensional chiral morphologies.

Block copolymer self-assembly has been proven to be a powerful tool for directing the feature size, morphology, and porosity of various functional inorganic materials on the mesoscale (*12*, *13*). In principle, this structural control provides an ideal platform for tuning and studying mesostructural effects on the superconducting properties of inorganic materials, but has not been exploited to date. To the best of our knowledge, the sole example in peer-reviewed literature involving block copolymers and superconductors describes the deposition of ferromagnetic/superconducting bilayers on a diblock copolymer substrate (*14*). In contrast, here, we demonstrate the use of block copolymer self-assembly to structure direct a superconductor, niobium nitride (NbN), into films of periodically ordered mesoporous materials, with the alternating gyroid (G^A) morphology exhibiting a superconducting transition at 7 to 8 K. We expect this study to pave the way toward investigations of superconductors with a plethora of block copolymer self-assembly–directed mesostructures.

RESULTS AND DISCUSSION

We used two triblock terpolymers—poly(isoprene)-*block*-poly(styrene)-*block*-poly(ethylene oxide) with a molar mass of 63.8 kg mol^{-1} (ISO-64k) and poly(isoprene)-*block*-poly(styrene)-*block*-poly(ethylene oxide) with a molar mass of 86.2 kg mol^{-1} (ISO-86k)—to structure direct sol-gel–derived niobium oxide (Nb_2O_5) into three-dimensional G^A network structures by solvent evaporation–induced self-assembly (Fig. 1) (*15*). Block copolymer–directed co-continuous cubic gyroid structures usually consist of two interpenetrating network subvolumes that are related to each other by an inversion operation (*16*). If these two minority networks are constituted by the same block (for example, in AB diblock copolymers), the structure is referred to as a double gyroid (G^D; $Ia\bar{3}d$) (*16*). In the case pursued here, where the two minority subvolumes are made up of different blocks (that is, the A and C end blocks in ABC triblock terpolymers; blue and green blocks/volumes in Fig. 1), the resulting chiral structure is called G^A (or single gyroid) ($I4_132$) and lacks an inversion center in its unit cell (*16*). The chemical structures of the ISO terpolymers and inorganic sol-gel precursors used in this study are depicted in Fig. 1B (top), together with a schematic of the synthesis approach and evolution of the G^A structure during different processing steps (Fig. 1B, bottom).

Superconducting NbN has previously been synthesized by nitriding sol-gel–derived Nb_2O_5 fibers (*17*). The resulting materials were not mesoporous and required a nitriding temperature of 1050°C to exhibit superconductivity. Finding appropriate thermal treatments of block copolymer–directed mesoporous inorganic materials is typically a balance between optimizing structure preservation (by reducing processing temperatures) and improving material properties (by increasing processing temperatures). At 1050°C, the mesostructure of the present block copolymer self-assembly–directed materials

[1]Department of Materials Science and Engineering, Cornell University, Ithaca, NY 14853, USA. [2]Department of Chemistry and Chemical Biology, Cornell University, Ithaca, NY 14853, USA. [3]Department of Physics, Cornell University, Ithaca, NY 14853, USA. [4]Cornell High Energy Synchrotron Source, Cornell University, Ithaca, NY 14853, USA. [5]Kavli Institute at Cornell for Nanoscale Science, Cornell University, Ithaca, NY 14853, USA.
*These authors contributed equally to this work.
†Present address: Simpson Querrey Institute for Bionanotechnology, Northwestern University, Evanston, IL 60208, USA.
‡Present address: Low Energy Electronic Systems IRG, Singapore-MIT Alliance for Research and Technology, Singapore 138602, Singapore.
§Corresponding author. E-mail: ubw1@cornell.edu

collapsed (fig. S1). A lower nitriding temperature of 600°C (*18*), or even 700°C, retained the mesostructure well, but the resulting materials were not superconducting. Numerous heating profiles were explored to strike a balance between superconductivity and the retention of an ordered mesoporous structure. Ultimately, a two-step nitriding procedure—consisting of first nitriding at 700°C, then cooling to room temperature, and finally renitriding at either 850° or 865°C—was necessary to successfully generate periodically ordered mesoporous nitrides that exhibited a superconducting transition. Although materials nitrided in a single step at 850°C retained ordered mesoporosity, they were not superconducting.

After solution casting and solvent evaporation, the terpolymers were removed by calcination in air at 450°C, yielding freestanding single-network G^A mesoporous films of amorphous Nb_2O_5. The Nb_2O_5 G^As were converted into films of gyroidal mesoporous superconducting NbN by heating under flowing gaseous ammonia in two steps: first to 700°C and subsequently to 850°C for ISO-64k and 865°C for ISO-86k. The materials at different processing steps are depicted in Fig. 1. The as-made hybrids exhibit a yellow/brown shade that disappears for the oxides upon calcination to 450°C. Nitrided samples appear as black and metallic shining solids. The materials remain close to their original shape with only a few cracks, rather than disintegrating into many pieces or even powders upon heat treatments.

Small-angle x-ray scattering (SAXS) was used to quantitatively characterize the mesostructural periodic order of ISO-64k/ISO-86k–derived materials (Fig. 2, A and B) at various processing stages (*12*). The SAXS patterns for as-made block copolymer–oxide hybrid materials (Fig. 2, A and B, bottom) are consistent with the G^A morphology and with a d_{100} unit cell size of 52.3 nm for ISO-64k and 61.8 nm for ISO-86k. After calcining in air at 450°C (Fig. 2, A and B, second from the bottom), the patterns remain consistent with the G^A morphology, but the peaks shift to higher q values and broaden, with a d_{100} spacing of 37.2 nm for ISO-64k and 49.5 nm for ISO-86k. Peak broadening indicates some loss of the long-range order of the mesoscale structure. The corresponding lattice shrinkage is typical during the removal of organic materials and the condensation/crystallization of inorganic materials in block copolymer–oxide systems (*18*). After nitriding under ammonia first at 700°C and then at 850°/865°C, the SAXS patterns continue to shift to higher q values and to broaden (Fig. 2, A and B, second from the top and top). The 700°C samples have a d_{100} spacing of 30.7 nm for ISO-64k and 43.8 nm for ISO-86k. Although the ISO-86k–derived sample treated at 865°C shows higher-order reflections consistent with a G^A lattice and a d_{100} spacing of 35.7 nm, the ISO-64k–derived sample brought to 850°C only shows one reflection, making structural lattice assignment by SAXS alone impossible. Assuming a G^A lattice, the corresponding d_{100} spacing from the first-order reflection would be 27.0 nm. Using block copolymers

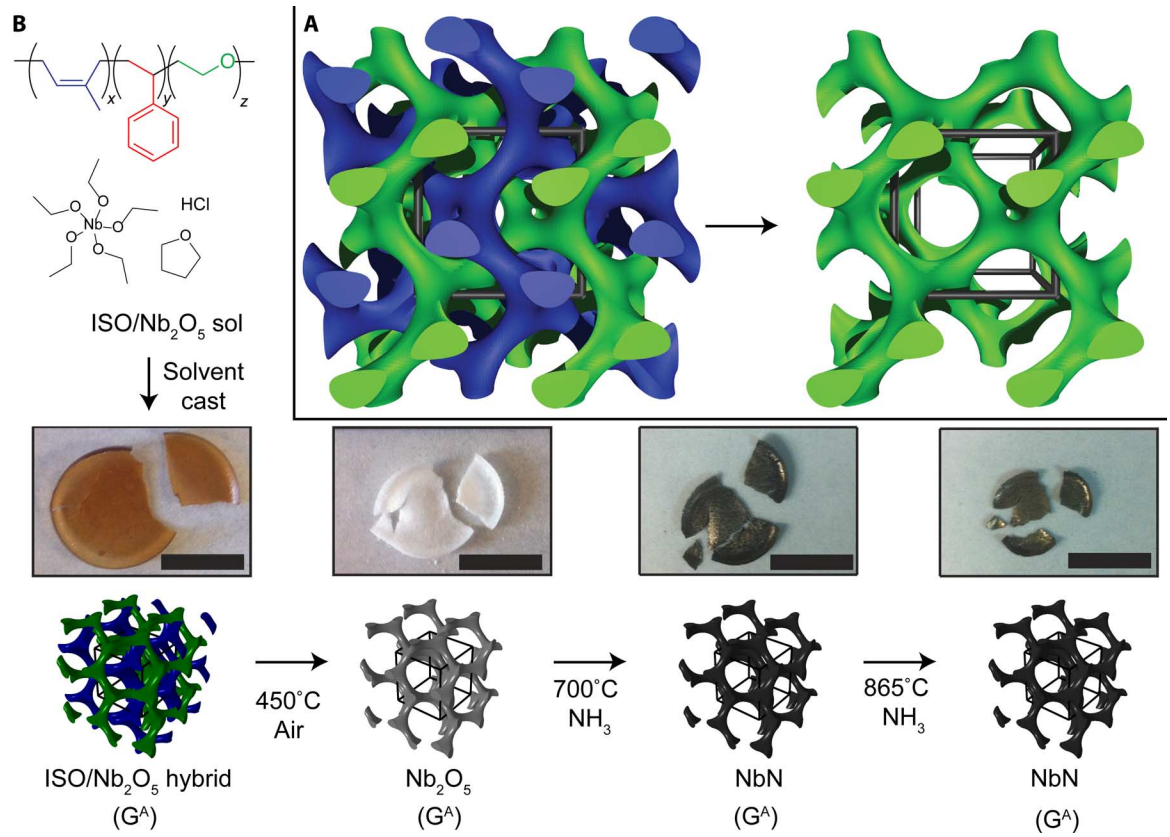

Fig. 1. G^A structure and sample/structure evolution from initial compounds to final NbN superconductors. (**A**) G^A before and after processing, with the unit cell indicated by the black cube. (**B**) (Top) Chemical structures of compounds and (bottom) schematic of synthesis and processing steps with photographs of the final materials. Block terpolymers (ISO) are combined with the Nb_2O_5 sol-gel precursors in a common solvent. Hybrid block copolymer/Nb_2O_5 G^A structures are generated by solvent evaporation–induced self-assembly. After calcination in air, the mesoporous Nb_2O_5 G^As are transformed to NbN G^As in a two-step nitriding process. Scale bars in all photographs represent 1 cm. NH_3, ammonia.

with different molar masses therefore enables tuning of the lattice parameters of the periodic self-assembly structures. In all samples, except for the ISO-64k–derived 850°C nitride, a significant orientation of the mesostructure was observed, as indicated by spots in the two-dimensional SAXS patterns (figs. S2 and S3).

To corroborate the structural assignments from SAXS and to provide real space images of the structural sample evolution, we used scanning electron microscopy (SEM) to characterize the mesoscale morphology of the materials obtained at different processing stages. SEM images of ISO-64k– and ISO-86k–derived samples are shown in Fig. 3 and fig. S4. It is evident that, as the materials progress through the heat treatments and shrink, they never completely lose their periodic order. Both final nitrides exhibit projections with four- and sixfold pore symmetry, as expected for the cubic G^A morphology, further corroborating the structural assignments (figs. S5 and S6). Despite experiencing heat treatments up to 865°C, the materials remained mesoporous, rather than structurally collapsing.

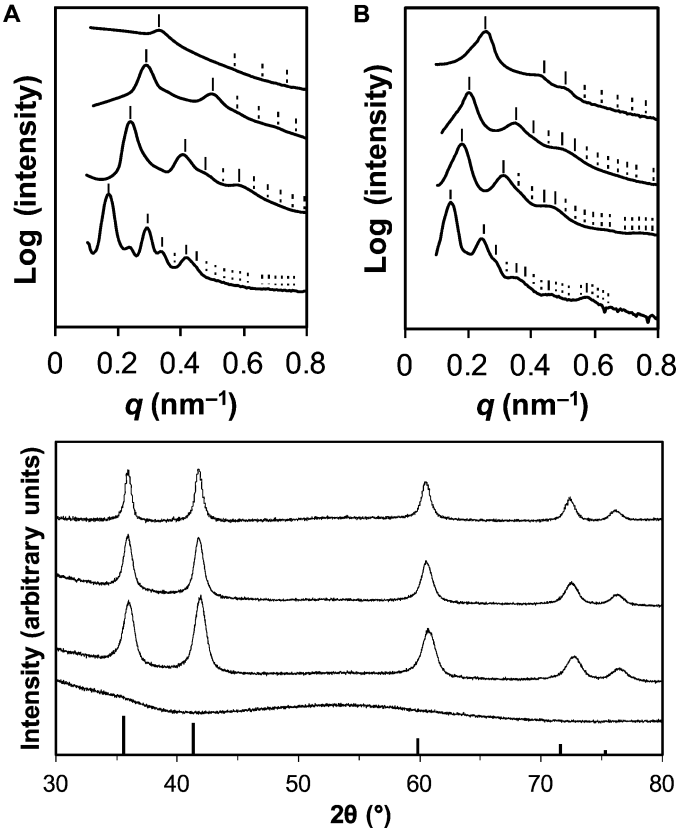

Fig. 2. Materials characterization by x-ray scattering. (**A** and **B**) SAXS patterns of samples derived from ISO-64k (A) and ISO-86k (B) at various processing stages. From bottom to top: ISO/oxide hybrids; samples calcined at 450°C in air; samples nitrided at 700°C; and sample nitrided at 850°/865°C. Observed (solid) and expected (dashed) peak positions for the G^A structure are indicated by ticks above each curve. Curves for the ISO-86k–derived samples were integrated using a selected angular range as a result of the significant orientation of the mesostructure. (**C**) Powder XRD patterns of samples at various processing stages. From bottom to top: Sample calcined at 450°C in air; sample nitrided at 700°C; sample nitrided at 850°C; and sample nitrided at 865°C. All patterns are from samples derived from ISO-64k, except for the top trace, which is from a sample derived from ISO-86k. Bottom tick marks indicate expected peak positions and relative intensities for a cubic rock salt NbN pattern (Powder Diffraction File card 04-008-5125).

Porosity was established and pore size distributions were obtained by analysis of N_2 sorption measurements performed on powders of ISO-64k–derived samples calcined at 450°C, nitrided at 700°C, and nitrided at 850°C. The isotherms (fig. S7) exhibit typical type IV curves with H_1-type hysteresis (*18*, *19*). In all cases, as expected, the surface area is dominated by mesoporosity (diameters of 2 to 50 nm) rather than microporosity (diameters <2 nm). In Fig. 3A, $dV/d\log(w)$–versus–pore width (where V is pore volume and w is pore width) is plotted for the three different samples, showing a decrease in average Barrett-Joyner-Halenda model pore sizes from 31 to 21 to 16 nm with increasing processing temperature. Resulting surface areas and pore volumes are summarized in table S1. Brunauer-Emmett-Teller model surface areas decrease from 111 to 86 to 59 $m^2 g^{-1}$, whereas pore volumes decrease from 1.01 to 0.71 to 0.41 $cm^3 g^{-1}$ for samples treated at 450°, 700°, and 850°C, respectively. These results are consistent with the observations of structural shrinkage from SAXS and SEM and corroborate open and accessible mesoporosity. As an example, assuming a bulk density of 8.47 g cm^{-3} for the nitride and using the N_2 sorption–derived pore volume, the sample treated at 850°C had 77.5% porosity.

The atomic crystal structure of the materials at different processing stages was characterized using powder x-ray diffraction (XRD) (Fig. 2C). After calcination, the block copolymer–directed oxides yielded amorphous Nb_2O_5 (Fig. 2C, bottom). Nitriding at 700°C for 12 hours leads to material crystallization into a cubic rock salt structure characteristic of many binary metal nitrides, including NbN. Upon analysis of XRD data, the cubic lattice parameter for this material was found to be 4.31 Å. After further nitriding in the second step at 850°C (Fig. 2C, second to top trace), the materials retained the rock salt structure, but the lattice parameter increased to 4.33 Å. After further nitriding at 865°C instead of 850°C (Fig. 2C, top trace), the lattice parameter remained at 4.33 Å. The lattice parameters for the 850° and 865°C nitrided samples are similar to those measured by Nomura *et al.* (*17*) using the same nitriding temperature for macroscopic Nb_2O_5 fibers but are smaller than that of pure bulk cubic NbN (*17*, *20*). We attribute this difference in lattice parameter to residual oxygen content and anion vacancies, consistent with a lattice parameter–based compositional estimate based on Vegard's law (fig. S8). Nomura *et al.* (*17*) did not observe the rock salt structure in NbN fibers until nitriding at 800°C (and superconductivity was first observed at 1050°C). We attribute the ability to generate a cubic crystal structure in our mesostructured materials at lower temperatures to the porosity of the gyroidal Nb_2O_5 film and the resulting short solid-state diffusion lengths for oxygen and nitrogen atoms to reach a reactive solid-pore interface. The coherent scattering domain size, determined from a Debye-Scherrer analysis of x-ray peak widths, was found to be 7.2 nm in the 700°C nitrided ISO-64k–derived material. After further nitriding at 850°C, the domains grew to 9.0 nm. In the 865°C nitrided ISO-86k–derived sample, the domain size was approximately 13.6 nm. These domain sizes are considerably smaller than the unit cell mesopore repeat but are comparable to the pore wall diameter, consistent with structure retention upon thermal processing even at the highest temperature. The pore wall diameters were measured by SEM image analysis and were found to be 9.9 ± 1.5 nm for the 700°C ISO-64k–derived nitride, 10.5 ± 1.5 nm for the 850°C ISO-64k–derived nitride, and 15.2 ± 3.1 nm for the 865°C ISO-86k–derived nitride. High-resolution transmission electron microscopy (TEM) images of the final ISO-64k– and

ISO-86k–derived materials (figs. S9 to S11) confirm this observation and exhibit a (200) plane spacing of 2.2 Å, comparable to the lattice parameter measured by XRD.

We characterized the magnetization behavior of our materials at low temperatures. The zero-field–cooled temperature-dependent magnetization was measured for film samples of 850°C nitrided materials, with their long axis oriented either parallel or perpendicular to the applied magnetic field (Fig. 4A). Both geometries show a superconducting transition with a similar trend: a critical temperature (T_c) of 7.8 K and a broad transition down to 2.5 K. Nitrided samples treated at 865°C behaved similarly (Fig. 4B). The observed T_c is below that of pure bulk NbN (16 K) (*17*, *20*). Samples with their long axis oriented perpendicular to the applied magnetic field have larger demagnetization than the parallely oriented samples, which is expected given the aspect ratio (~10) of the films. The perpendicularly oriented sample was also temperature-swept to 30 K to ensure that no changes occurred between 10 and 30 K (fig. S12). Field-cooled magnetization data are comparable to the zero-field–cooled data (fig. S13). In addition, the parallely oriented sample was zero-field–cooled to 2.5 K, and its low field–dependent magnetization was measured to estimate the flux exclusion and critical current (J_c) of the material (fig. S14). Samples nitrided in single steps to only 700° or 850°C did not exhibit a superconducting transition.

From the slope of the field-dependent magnetization at low fields (fig. S14) and using the fractional density of the material calculated from the N_2 sorption data, the flux exclusion was calculated to be 5% compared to a dense, perfect superconductor with the same outer dimensions. This

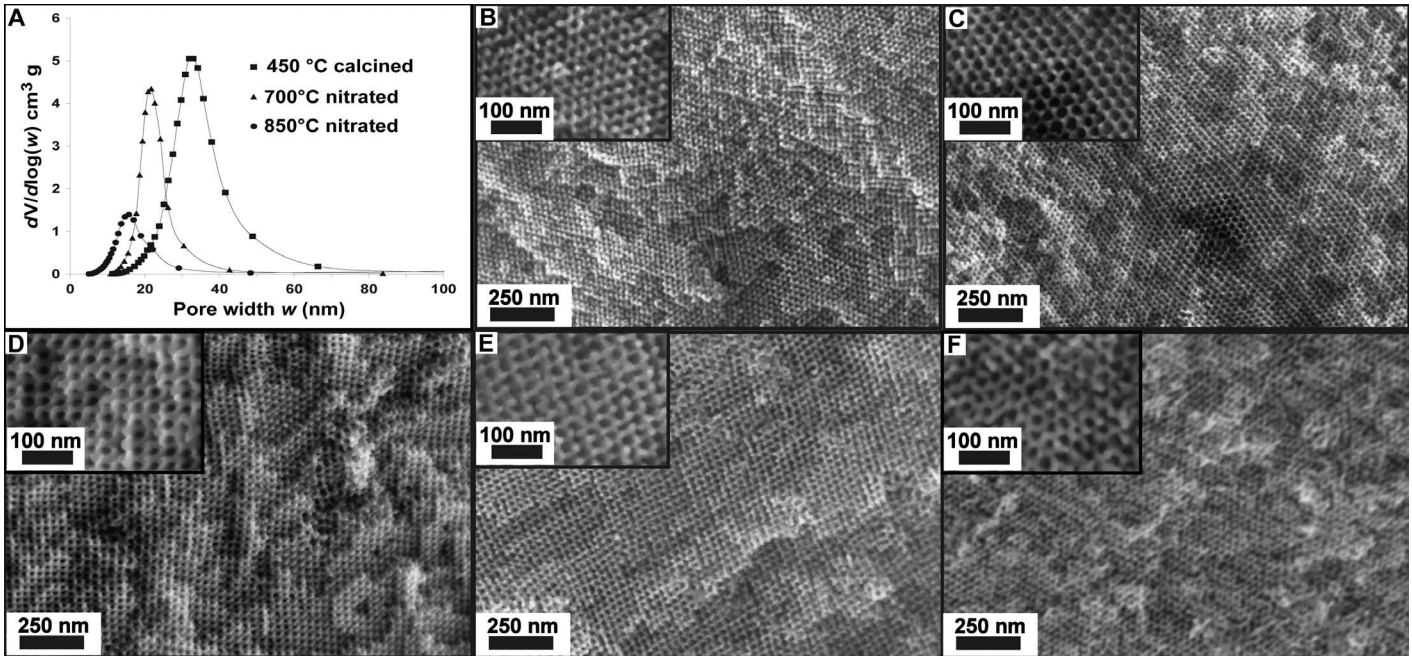

Fig. 3. Materials characterization by N_2 sorption and SEM. (**A**) Pore size distributions from N_2 sorption measurements for ISO-64k–derived samples at various processing stages. (**B** to **F**) SEM images of mesoporous samples at different processing stages. ISO-64k–derived gyroidal NbN (B) after nitriding at 700°C and (C) after nitriding at 850°C. (D) ISO-86k–derived gyroidal Nb_2O_5 after calcination at 450°C in air. ISO-86k–derived gyroidal NbN (E) after nitriding at 700°C and (F) after nitriding at 865°C.

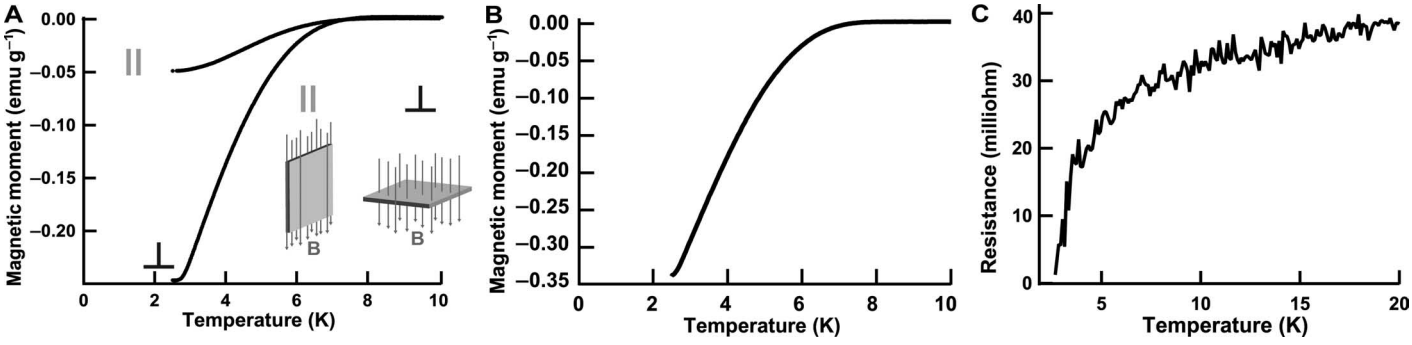

Fig. 4. Magnetization and electrical resistance of superconducting gyroids. (**A**) Temperature-dependent magnetization from 2.5 to 10 K for ISO-64k–derived NbN films in an applied field of 200 Oe, with their long axis oriented either parallel (top; ||) or perpendicular (bottom; ⊥) to the applied field (see insets for the different geometries tested). (**B**) Temperature-dependent magnetization from 2.5 to 10 K for ISO-86k–derived NbN films in an applied field of 100 Oe, with their long axis oriented perpendicular to the field. (**C**) Temperature-dependent four-point electrical resistance of ISO-86k–derived NbN films showing a drop beginning at approximately 7 K.

suggests that the flux lines are not perfectly excluded from the perimeter of the sample and may be passing through the mesopores. The field-dependent magnetic moment exhibits changes in slope at around −19.8 and −33.7 kOe (fig. S15). These fields correspond well to one flux quantum per pore on a ~33 nm lattice and to two flux quanta per pore on a ~35 nm lattice, respectively. Assuming a Bean model interpretation (*21*, *22*), the subtle increases in magnetization at these fields indicate an increase in critical current due to pinning of the flux quanta. Additional SAXS experiments showed that some fractions of a sample of the same batch processed under identical conditions indeed have mesoscale repeat distances of 33.0 nm (fig. S16). This degree of heterogeneity is not surprising in light of the substantial shrinkage (>50% for ISO-86k) that samples undergo during processing. The critical current density (J_c) was estimated to be 440 A cm^{-2} at 100 Oe and 2.5 K. This relatively low value (*20*) may indicate weak links such as cracks or grains of poor superconductivity through the film thickness.

The electrical conductivity and resistance of the samples were characterized by two techniques: room-temperature two-point conductivity of an ISO-64k–derived sample after the final nitridation at 850°C and four-point temperature-dependent resistance measurements of an ISO-86k–derived sample after final nitridation at 865°C. In the two-point resistance measurement, the sample was found to have a conductivity of 4.0 S cm^{-1} at room temperature, similar to values previously measured for mesoporous mixed transition metal nitrides that were generated by nitriding oxides (*18*). In the four-point measurement, the electrical resistance of an ISO-86k–derived film after all processing steps was measured as a function of temperature from 300 to 2 K. As shown in Fig. 4C, the material exhibited a dramatic drop in electrical resistance at approximately 7 K, consistent with the behavior expected for a superconductor and the T_c values observed in magnetometry.

As noted above, the T_c of 7 to 8 K for the mesoporous superconducting materials is below the T_c of pure, bulk NbN, which is around 16 K. Nonstoichiometry, different crystal structures, oxygen content, atomic vacancies, and small feature sizes can all lower or suppress the T_c in NbN (*17*, *23*–*28*). The experimental T_c and lattice parameters for the mesoporous superconducting materials studied here are consistent with the values for a composition $NbN_{1-x}O_y\,\square_{x-y}$ (where □ represents vacancies) rather than for a highly stoichiometric δ-NbN [(*20*, *28*–*30*); see also fig. S8]. This is not surprising considering the use of the nitride precursor Nb_2O_5 and relatively low nitriding temperatures. For the present system, the nitriding temperatures necessary to generate superconducting materials (at least 850°C) were within the same range in which a loss of the long-range periodic order of the G^A mesostructure occurred. In future studies, as processing steps for block copolymer self-assembly–directed mesoporous superconductors are optimized, we anticipate higher-quality structural control of superconducting samples.

CONCLUSION

Block copolymer self-assembly is considered a hallmark of soft condensed matter physics. Owing to structural versatility, as well as precise tunability of morphology, dimensionality, and feature size, block copolymer self-assembly–directed inorganic mesostructure formation is an ideal platform for studying periodically ordered mesostructural effects on superconducting properties. Generating such ordered mesoporous superconductors is not limited to NbN or to the particular synthetic strategy shown in this work. For example, block copolymer self-assembly could be used to tailor-make periodically ordered mesoporous superconductors by selective block etching and subsequent metal (*31*) or metal oxide (*32*) backfilling, or by block copolymer–directed self-assembly of superconducting oxides. Periodic ordering of superconductors on the mesoscale may be expected to lead to a host of novel properties and applications. For example, pinning of superconducting vortex lines on the periodic mesostructure may be expected to lead to commensurate-incommensurate transitions with applied magnetic field intensity, to angle-dependent forces as the vortex lines align with the pore axes, and to vortex avalanches (*33*–*35*). The chiral nature of some mesostructured superconductors will likely only couple weakly to the underlying superconducting pairing (*36*) but may give rise to unusual bulk material properties such as nonlinear coupling to magnetic fields (*37*). These properties may be expected to be of higher magnitude than those of chiral molecular systems because the London penetration depth (for example, 39 nm for Nb and 370 nm for NbN) (*38*, *39*) is comparable to the chiral superstructure repeat distance. Finally, backfilling of mesopores with second material components should allow for the leveraging of enormous surface areas to enhance interfacial superconductivity between nonsuperconducting constituents. Such studies were previously restricted to planar interfaces between nonsuperconducting constituents, including metal-metal interfaces (*40*), metal-semiconductor interfaces (*41*, *42*), metal-insulator interfaces (*43*), semiconductor-semiconductor interfaces (*19*, *44*), and insulator-insulator interfaces (*45*, *46*). Mesostructured interfaces introduce topological degrees of freedom to the field of interfacial superconductivity. Obviously, much of this is speculation, because no one hitherto has ever produced a mesoporous superconducting material with a three-dimensionally continuous chiral cubic mesostructure. Moving forward, block copolymer self-assembly–directed superconductors may provide a fertile area for the study of superconductivity and the effects of periodic and chiral mesostructural order on superconducting properties.

MATERIALS AND METHODS

Materials

Hydrochloric acid (37 wt %; American Chemical Society/National Formulary/Food Chemicals Codex grade), niobium(V) ethoxide (99.999%; metals basis), and anhydrous tetrahydrofuran (THF) (≥99.9%; inhibitor-free) were all used as received. Anhydrous ammonia (99.9%; premium grade) was purified over a SAES MicroTorr MC400-702F purifier to remove residual oxygen and moisture.

Two poly(isoprene)-*block*-poly(styrene)-*block*-poly(ethylene oxide) block copolymers were synthesized by sequential anionic polymerization using known procedures (*47*, *48*). The block copolymer composition and the polydispersity index (PDI) were characterized by a combination of size exclusion chromatography (gel permeation chromatography) and nuclear magnetic resonance. ISO-64k had an overall molar mass of 63.8 kg mol^{-1} and a PDI of 1.03. It was composed of polyisoprene 18.7 kg mol^{-1}, polystyrene 40.5 kg mol^{-1}, and poly(ethylene oxide) 4.6 kg mol^{-1}. ISO-86k had an overall molar mass of 86.2 kg mol^{-1} and a PDI of 1.09. It was composed of polyisoprene 22.7 kg mol^{-1}, polystyrene 58.7 kg mol^{-1}, and poly(ethylene oxide) 4.7 kg mol^{-1}.

Synthesis of mesoporous NbN

Seventy-five milligrams of ISO-64k was dissolved in 2 ml of anhydrous THF. The Nb_2O_5 sol was prepared through a hydrolytic sol-gel route.

First, 0.51 ml (2.03 mmol) of niobium(V) ethoxide was quickly added to 0.30 ml of HCl in 1.00 ml of THF and stirred vigorously in a 4-ml vial. After 5 min, 1.00 ml (12.3 mmol) of THF was quickly added to the stirring vial. After 2 min, an aliquot of the transparent yellow sol was added to the polymer solution. The sol aliquot used was 0.24 ml per 75 mg of ISO-64k to generate a G^A morphology. For the ISO-86k–derived samples, a similar procedure was used with 100 mg of ISO-86k dissolved in 4 ml of anhydrous THF. The sol was prepared as for the ISO-64k–derived samples, with a sol aliquot of 0.31 ml per 100 mg of ISO-83k to generate a G^A morphology.

The ISO/oxide mixtures were stirred vigorously for at least 3 hours. Films were then cast in polytetrafluoroethylene (PTFE) dishes. For the ISO-64k samples, the solvent was evaporated with the PTFE dish on a glass petri dish covered by a glass dome, on a hot plate set to 50°C overnight. For the ISO-86k–derived samples, the solvent was evaporated with the PTFE dish on a glass petri dish covered by a glass dome with continuous dry nitrogen purge, on a hot plate set to 35°C for 24 to 48 hours. Films were subsequently aged at 130°C for 2.5 hours in a vacuum oven. To remove any closed layers on the polymer/oxide hybrid films, we treated the films with CF_4 plasma in an Oxford Plasmalab 80+ Reactive Ion Etcher system at 300 W for 40 min on each side of the film. Films were calcined in air to generate freestanding mesoporous oxides in a flow furnace: ramped by 1°C min^{-1} to 450°C and held for 3 hours at 450°C, and allowed to cool to ambient temperature.

For nitriding of the resulting oxides, films were heated in a flow furnace under anhydrous ammonia gas in two heating steps. In the first step, the oxide samples were heated under flowing ammonia gas at a flow rate of 2.5 liter $hour^{-1}$ and at a heating ramp rate of 350°C $hour^{-1}$ up to 700°C, with a dwell time of 12 hours at 700°C. The tube was cooled to room temperature under flowing ammonia and purged with N_2. One tube valve was opened to air for 30 min, then the tube end was removed and the samples were removed from the tube. In the second step, samples were heated again under flowing ammonia gas at a flow rate of 2.5 liter $hour^{-1}$ and at a heating ramp rate of 350°C $hour^{-1}$ up to 850° or 865°C, with a dwell time of 3 hours at 850°/865°C. The tube was cooled to room temperature under flowing ammonia and purged with N_2. One tube valve was opened to air for 30 min, then the tube end was removed. Finally, samples were removed for characterization. The resulting freestanding mesoporous films were around 160 μm thick, with lengths and widths around 5 mm.

Magnetization characterization

Magnetization measurements were performed on a Quantum Design Physical Property Measurement System equipped with a 9-T superconducting magnet (model PPMS-9T), using the vibrating sample magnetometer setup. For samples in the configuration perpendicular to the magnetic field geometry, small flakes (lengths and widths around 1.5 mm) of the mesoporous films with a mass of 1 to 2 mg were mounted on a fused quartz cylinder using Lake Shore Cryotronics IMI 7031 low-temperature varnish. The quartz cylinder was then loaded into a gold-coated brass half tube holder. For samples in the configuration parallel to the magnetic field geometry, flakes were mounted on a fused quartz paddle holder using Lake Shore Cryotronics IMI 7031 low-temperature varnish. Samples were zero-field–cooled to 2.5 K. When the temperature had stabilized, a magnetic field of 200 Oe was applied. The samples were then heated from 2.5 to 10 K at a rate of 0.15 K min^{-1} while the magnetic moment of the samples in a field of 200 Oe was being measured.

For characterization of field-cooled magnetization (fig. S13), the sample was cooled to a temperature of 2 K under an applied field of 50 Oe. The sample was then heated from 2 to 30 K at a rate of 1 K min^{-1} while measuring the magnetic moment.

Samples measured up to 30 K in the perpendicular configuration were zero-field–cooled to 2.5 K. A field of 70 Oe was applied, and the temperature was swept to 15 K at a rate of 0.5 K min^{-1}, then to 300 K at a rate of 20 K min^{-1} (only values from 2.5 to 30 K were plotted in fig. S12).

The flux exclusion was calculated from the susceptibility determined from the initial slope of a field-dependent magnetization measurement performed on an ISO-64k–derived nitride at 2.5 K (fig. S14). The reported critical current (J_c) was calculated from the low field–dependent magnetization of an ISO-64k–derived nitride using the Bean critical state model (*21*) at 2.5 K and 100 Oe. The mesoporosity of the sample was not taken into account in the calculation of the flux exclusion and critical current because of the lack of an appropriate model. The values reported are compared to those of a dense NbN solid.

For characterization of high-field magnetization, a sample of the final ISO-86k–derived 865°C nitride was mounted in a polypropylene capsule (Quantum Design) in a Quantum Design Physical Property Measurement System vibrating sample magnetometer and cooled to 2.5 K. A field of 100 Oe was applied to locate the sample, then the magnetic moment was measured as a function of applied field during a sweep (10 Oe s^{-1}) first from 0 to 50 kOe, then from 50 to −50 kOe, and finally from −50 to 0 kOe. The points of slope change reported were determined from the intersection points of linear fits to the data, as shown in fig. S15.

XRD characterization

Powder XRD data for the oxide and nitrides were collected on a Rigaku Ultima IV diffractometer equipped with a D/teX Ultra detector, using CuK_α radiation and a scan rate of 2° min^{-1}. Lattice parameters of the NbN samples were calculated from $2d_{200}$ ($2\theta \approx 42°$). The crystallite sizes reported are the lower limits of the coherent scattering domain size, as determined from a Debye-Scherrer analysis of all five peaks between 30° and 80°. Instrumental and other sources of peak broadening were not accounted for in this analysis but are not expected to have a significant effect given the small size of the coherent scattering domains observed.

SAXS characterization

SAXS patterns were obtained on either a home-built beamline equipped with a Rigaku RU-3HR copper rotating anode generator, a set of orthogonal Franks focusing mirrors and a phosphor-coupled charge-coupled device (CCD) detector (as described in detail elsewhere) (*49*), or at the G1 station of the Cornell High Energy Synchrotron Source (CHESS) with a typical beam energy of 10.5 keV and a sample-to-detector distance of 2.6 m or more. The two-dimensional patterns obtained from a point-collimated beam were azimuthally integrated using the Nika software package (*50*) to yield the one-dimensional plots shown in Fig. 2. The ISO-64k oxide pattern (fig. S2) and ISO-86k nitride pattern (fig. S16) were collected at the Cornell High Energy Synchrotron Source, whereas all other patterns were collected on the home-built beamline. The ISO-86k data exhibited a significant orientation of the mesostructure and were integrated azimuthally over a selected angular range of 197° to 331° for the hybrid, 57.5° to 92.5° for the 700°C nitride, and 88.5° to 103.5° for the 865°C nitride. The two-dimensional data are shown in fig. S3.

SEM characterization

Fractured and powdered monolith samples were directly mounted on stubs using carbon tape. Oxide samples were coated with Au-Pd to

increase conductivity, whereas nitride samples required no coating. The samples were characterized by SEM on a TESCAN MIRA3 LM field-emission scanning electron microscope and on a Zeiss LEO 1550 field-emission scanning electron microscope equipped with in-lens detectors. Pore wall thickness was measured using ImageJ software, taking the average of 100 measurements on each image. Uncertainties in pore wall thickness are reported as the standard deviation of the same set of 100 measurements. Fourier transforms shown in figs. S5 and S6 were calculated with ImageJ software.

TEM characterization

After the final heat treatment, powdered monoliths were drop-cast from isopropyl alcohol on carbon-coated copper TEM grids (Electron Microscopy Sciences Inc.). The samples were imaged by standard TEM on an FEI Tecnai T12 at an accelerating voltage of 120 kV. High-resolution TEM images were acquired on an FEI Tecnai F20 at an accelerating voltage of 200 kV. Lattice parameters were determined by Fourier transforms of high-resolution TEM images.

Characterization of low-temperature conductivity

After all heat treatments, a piece of the ISO-86k–derived nitride was used for a four-point resistance measurement. Contacts were made on the sample using EPO-TEK H20E silver-filled epoxy and were connected via a carrier chip to a Quantum Design Physical Property Measurement System resistivity puck (fig. S17). The carrier chip was used to mechanically isolate the sample to prevent cracking during cooling. It consists of four sputtered gold contact pads on a 100-nm thermal oxide layer atop a (100) silicon substrate. The sample was electrically connected to the pads using EPO-TEK H20E, and the pads were then wire-bonded to the Physical Property Measurement System contacts. The excitation current was 25 μA. Because of the sample's mesoporosity, the cross-sectional area was not estimated, and the values reported are resistance, not resistivity.

Characterization of room-temperature conductivity

After all heat treatments, a piece of a nitride was used for a two-point conductivity measurement. A portion of the sample's top surface was masked and Au-Pd–coated to generate contacts. The mask was removed, and drops of In-Ga liquid metal eutectic were placed on the Au-Pd contacts. Resistance was measured across the known cross section of the sample and was used to calculate conductivity. Mesoporosity was not taken into account in the conductivity calculations, which provide a lower bound for the conductivity of the sample.

N_2 sorption characterization

N_2 sorption characterization was performed on a Micromeritics ASAP 2020 surface area and porosity analyzer at −196°C. The powdered samples were degassed at 120°C under vacuum for at least 6 hours before measurements. Surface areas were determined using the Brunauer-Emmett-Teller method (*51*), and pore size distributions were calculated using the Barrett-Joyner-Halenda method (*52*).

SUPPLEMENTARY MATERIALS

Supplementary material for this article is available at http://advances.sciencemag.org/cgi/content/full/2/1/e1501119/DC1

Fig. S1. Cross-sectional SEM images of ISO-64k–derived material nitrided in one step at 1050°C.
Fig. S2. Two-dimensional SAXS patterns of ISO-64k–derived samples at various processing stages.
Fig. S3. Two-dimensional SAXS patterns of ISO-86k–derived samples at various processing stages.
Fig. S4. SEM images of ISO-64k–derived mesoporous samples at different processing stages.
Fig. S5. Cross-sectional SEM images of an ISO-64k–derived monolith after final nitriding at 850°C.
Fig. S6. Cross-sectional SEM images of an ISO-86k–derived monolith after final nitriding at 865°C.
Fig. S7. N_2 adsorption/desorption isotherms for ISO-64k–derived powder samples calcined at 450°C, nitrided at 700°C, and nitrided at 850°C.
Fig. S8. XRD-derived lattice spacing as a function of nitriding temperature for NbN fibers [(*17*); black circles and fit] and our materials (red squares).
Fig. S9. TEM micrographs of nitrides derived from (A) ISO-64k and (B) ISO-86k after final heat treatments.
Fig. S10. High-resolution TEM micrograph of ISO-64k–derived nitride after final heat treatment.
Fig. S11. High-resolution TEM micrograph of ISO-86k–derived nitride after final heat treatment.
Fig. S12. Magnetization behavior of ISO-64k–derived 850°C gyroidal NbN material from 2.5 to 30 K, measured in a perpendicular orientation with an applied field of 70 Oe.
Fig. S13. Field-cooled magnetization behavior of ISO-86k–derived 865°C gyroidal NbN material from 2 to 30 K, measured in a perpendicular orientation with an applied field of 50 Oe.
Fig. S14. Field-sweeping magnetization behavior at 2.5 K of ISO-64k–derived NbN material heat-treated to 850°C.
Fig. S15. High-field magnetization behavior at 2.5 K of ISO-86k–derived NbN material heat-treated to 865°C.
Fig. S16. Two-dimensional (A) and integrated (B) SAXS patterns of ISO-86k–derived material processed in the same batch as that in fig. S3.
Fig. S17. Photograph of the four-point conductivity measurement apparatus.
Table S1. Surface area and pore volume (as measured by N_2 sorption) of ISO-64k–derived materials at different stages of thermal processing.

REFERENCES AND NOTES

1. R. Córdoba, T. I. Baturina, J. Sesé, A. Y. Mironov, J. M. De Teresa, M. R. Ibarra, D. A. Nasimov, A. K. Gutakovskii, A. V. Latyshev, I. Guillamón, H. Suderow, S. Vieira, M. R. Baklanov, J. J. Palacios, V. M. Vinokur, Magnetic field–induced dissipation-free state in superconducting nanostructures. *Nat. Commun.* **4**, 1437 (2013).
2. L. Piraux, X. Hallet, Artificial vortex pinning arrays in superconducting films deposited on highly ordered anodic alumina templates. *Nanotechnology* **23**, 355301 (2012).
3. U. Welp, Z. L. Xiao, J. S. Jiang, V. K. Vlasko-Vlasov, S. D. Bader, G. W. Crabtree, J. Liang, H. Chik, J. M. Xu, Superconducting transition and vortex pinning in Nb films patterned with nanoscale hole arrays. *Phys. Rev. B* **66**, 212507 (2002).
4. W. Vinckx, V. V. Moshchalkov, S. Mátéfi-Tempfli, M. Mátéfi-Tempfli, S. Michotte, L. Piraux, X. Ye, Vortex pinning in superconductors laterally modulated by nanoscale self-assembled arrays. *Physica C* **468**, 585–588 (2008).
5. A. Lungu, M. Bleiweiss, J. Amirzadeh, S. Saygi, A. Dimofte, M. Yin, Z. Iqbal, T. Datta, Superconductivity in nanostructured lead. *Physica C* **349**, 1–7 (2001).
6. Y.-J. Hsu, S.-Y. Lu, Y.-F. Lin, Nanostructures of Sn and their enhanced, shape-dependent superconducting properties. *Small* **2**, 268–273 (2006).
7. U.S. Department of Energy Basic Energy Sciences, "From quanta to the continuum: Opportunities for mesoscale science" (2012); available at www.meso2012.com.
8. E.-S. Jang, J.-J. Chang, J. Gwak, A. Ayral, V. Rouessac, L. Cot, S.-J. Hwang, J.-H. Choy, Asymmetric high-T_c superconducting gas separation membrane. *Chem. Mater.* **19**, 3840–3844 (2007).
9. C. Cirillo, M. Trezza, F. Chiarella, A. Vecchione, V. P. Bondarenko, S. L. Prischepa, C. Attanasio, Quantum phase slips in superconducting Nb nanowire networks deposited on self-assembled Si templates. *Appl. Phys. Lett.* **101**, 172601 (2012).
10. Y. Tsuchiya, Y. Mawatari, J. Ibuka, S. Tada, S. Pyon, S. Nagasawa, M. Hidaka, M. Maezawa, T. Tamegai, Flux avalanches in Nb superconducting shifted strip arrays. *Supercond. Sci. Technol.* **26**, 095004 (2013).
11. E. Culverwell, S. C. Wimbush, S. R. Hall, Biotemplated synthesis of an ordered macroporous superconductor with high critical current density using a cuttlebone template. *Chem. Commun.* **2008**, 1055–1057 (2008).
12. B. Smarsly, M. Antonietti, Block copolymer assemblies as templates for the generation of mesoporous inorganic materials and crystalline films. *Eur. J. Inorg. Chem.* **2006**, 1111–1119 (2006).
13. M. C. Orilall, U. Wiesner, Block copolymer based composition and morphology control in nanostructured hybrid materials for energy conversion and storage: Solar cells, batteries, and fuel cells. *Chem. Soc. Rev.* **40**, 520 (2011).
14. L. Ruiz-Valdepeñas, M. Velez, F. Valdés-Bango, L. M. Alvarez-Prado, F. J. Garcia-Alonso, J. I. Martin, E. Navarro, J. M. Alameda, J. L. Vicent, Imprinted labyrinths and percolation in Nd-Co/Nb magnetic/superconducting hybrids. *J. Appl. Phys.* **115**, 213901 (2014).

15. M. Templin, A. Franck, A. Du Chesne, H. Leist, Y. Zhang, R. Ulrich, V. Schädler, U. Wiesner, Organically modified aluminosilicate mesostructures from block copolymer phases. *Science* **278**, 1795–1798 (1997).
16. A. J. Meuler, M. A. Hillmyer, F. S. Bates, Ordered network mesostructures in block polymer materials. *Macromolecules* **42**, 7221–7250 (2009).
17. K. Nomura, Y. Takasuka, K. Kamiya, H. Nasu, Preparation of NbN fibres by nitridation of sol–gel derived Nb_2O_5 fibres. *J. Mater. Sci. Mater. Electron.* **5**, 53–58 (1994).
18. S. W. Robbins, H. Sai, F. J. DiSalvo, S. M. Gruner, U. Wiesner, Monolithic gyroidal mesoporous mixed titanium–niobium nitrides. *ACS Nano* **8**, 8217–8223 (2014).
19. K. Murase, S. Ishida, S. Takaoka, T. Okumura, H. Fujiyasu, A. Ishida, M. Aoki, Superconducting behavior in PbTe–SnTe superlattices. *Surf. Sci.* **170**, 486–490 (1986).
20. W. Martienssen, H. Warlimont, *Springer Handbook of Condensed Matter and Materials Data* (Springer, Berlin, 2006).
21. C. P. Bean, Magnetization of hard superconductors. *Phys. Rev. Lett.* **8**, 250–253 (1962).
22. C. P. Bean, Magnetization of high-field superconductors. *Rev. Mod. Phys.* **36**, 31–39 (1964).
23. E. K. Storms, A. L. Giorgi, E. G. Szklarz, Atom vacancies and their effects on the properties of NbN containing carbon, oxygen or boron—II: Superconducting transition temperature. *J. Phys. Chem. Solids* **36**, 689–694 (1975).
24. W. Lengauer, Characterization of nitrogen distribution profiles in fcc transition metal nitrides by means of T_c measurements. *Surf. Interface Anal.* **15**, 377–382 (1990).
25. J. R. Gavaler, M. A. Janocko, J. K. Hulm, C. K. Jones, Superconducting properties as a function of thickness in NbN films. *Physica* **55**, 585–591 (1971).
26. L. Kang, B. B. Jin, X. Y. Liu, X. Q. Jia, J. Chen, Z. M. Ji, W. W. Xu, P. H. Wu, S. B. Mi, A. Pimenov, Y. J. Wu, B. G. Wang, Suppression of superconductivity in epitaxial NbN ultrathin films. *J. Appl. Phys.* **109**, 033908 (2011).
27. U. Patel, S. Avci, Z. L. Xiao, J. Hua, S. H. Yu, Y. Ito, R. Divan, L. E. Ocola, C. Zheng, H. Claus, J. Hiller, U. Welp, D. J. Miller, W. K. Kwok, Synthesis and superconducting properties of niobium nitride nanowires and nanoribbons. *Appl. Phys. Lett.* **91**, 162508 (2007).
28. G.-I. Oya, Y. Onodera, Transition temperatures and crystal structures of single-crystal and polycrystalline NbN_x films. *J. Appl. Phys.* **45**, 1389–1397 (1974).
29. N. Terao, New phases of niobium nitride. *J. Less Common Met.* **23**, 159 (1971).
30. G. Brauer, Nitrides, carbonitrides and oxynitrides of niobium. *J. Less Common Met.* **2**, 131–137 (1960).
31. V. N. Urade, T.-C. Wei, M. P. Tate, J. D. Kowalski, H. W. Hillhouse, Nanofabrication of double-gyroid thin films. *Chem. Mater.* **19**, 768–777 (2007).
32. M. Kamperman, M. Nedelcu, C. Ducati, U. Wiesner, D.-M. Smilgies, G. E. S. Toombes, M. A. Hillmyer, S. Ludwigs, U. Steiner, H. J. Snaith, A bicontinuous double gyroid hybrid solar cell. *Nano Lett.* **9**, 2807–2812 (2009).
33. R. A. Webb, R. F. Voss, G. Grinstein, P. M. Horn, Magnetic field behavior of a Josephson-junction array: Two-dimensional flux transport on a periodic substrate. *Phys. Rev. Lett.* **51**, 690–693 (1983).
34. K. Harada, O. Kamimura, H. Kasai, T. Matsuda, A. Tonomura, V. V. Moshchalkov, Direct observation of vortex dynamics in superconducting films with regular arrays of defects. *Science* **274**, 1167–1170 (1996).
35. L. Civale, A. D. Marwick, T. K. Worthington, M. A. Kirk, J. R. Thompson, L. Krusin-Elbaum, Y. Sun, J. R. Clem, F. Holtzberg, Vortex confinement by columnar defects in $YBa_2Cu_3O_7$ crystals: Enhanced pinning at high fields and temperatures. *Phys. Rev. Lett.* **67**, 648–651 (1991).
36. X.-L. Qi, T. L. Hughes, S. Raghu, S.-C. Zhang, Time-reversal–invariant topological superconductors and superfluids in two and three dimensions. *Phys. Rev. Lett.* **102**, 187001 (2009).
37. M. Kauranen, J. J. Maki, T. Verbiest, S. Van Elshocht, A. Persoons, Quantitative determination of electric and magnetic second-order susceptibility tensors of chiral surfaces. *Phys. Rev. B* **55**, R1985–R1988 (1997).
38. B. W. Maxfield, W. L. McLean, Superconducting penetration depth of niobium. *Phys. Rev.* **139**, A1515 (1965).
39. D. E. Oates, A. C. Anderson, C. C. Chin, J. S. Derov, G. Dresselhaus, M. S. Dresselhaus, Surface-impedance measurements of superconducting NbN films. *Phys. Rev. B Condens. Matter* **43**, 7655–7663 (1991).
40. M. B. Brodsky, Superconductivity in an Ag-Pd-Ag epitaxial metal film sandwich. *Phys. Rev. B* **25**, 6060 (1982).
41. M. J. Burns, J. R. Lince, R. S. Williams, P. M. Chaikin, Electron localization and superconductivity in very thin epitaxially grown Ag films on Ge (001). *Solid State Commun.* **51**, 865–869 (1984).
42. R. Akihama, Y. Okamoto, Superconductivity in Au(10Å)/Ge(13Å) alternating ultra-thin layered films. *Solid State Commun.* **53**, 655–659 (1985).
43. A. Gozar, G. Logvenov, L. F. Kourkoutis, A. T. Bollinger, L. A. Giannuzzi, D. A. Muller, I. Bozovic, High-temperature interface superconductivity between metallic and insulating copper oxides. *Nature* **455**, 782–785 (2008).
44. N. Y. Fogel, E. I. Buchstab, Y. V. Bomze, O. I. Yuzephovich, M. Y. Mikhailov, A. Y. Sipatov, E. A. Pashitskii, R. I. Shekhter, M. Jonson, Direct evidence for interfacial superconductivity in two-layer semiconducting heterostructures. *Phys. Rev. B* **73**, 161306 (2006).
45. N. Reyren, S. Thiel, A. D. Caviglia, L. F. Kourkoutis, G. Hammerl, C. Richter, C. W. Schneider, T. Kopp, A.-S. Rüetschi, D. Jaccard, M. Gabay, D. A. Muller, J.-M. Triscone, J. Mannhart, Superconducting interfaces between insulating oxides. *Science* **317**, 1196–1199 (2007).
46. J. Mannhart, D. G. Schlom, Oxide interfaces—An opportunity for electronics. *Science* **327**, 1607–1611 (2010).
47. J. Allgaier, A. Poppe, L. Willner, D. Richter, Synthesis and characterization of poly[1,4-isoprene-*b*-(ethylene oxide)] and poly[ethylene-*co*-propylene-*b*-(ethylene oxide)] block copolymers. *Macromolecules* **30**, 1582–1586 (1997).
48. S. C. Warren, F. J. DiSalvo, U. Wiesner, Nanoparticle-tuned assembly and disassembly of mesostructured silica hybrid. *Nat. Mater.* **6**, 156–161 (2007).
49. A. C. Finnefrock, R. Ulrich, G. E. S. Toombes, S. M. Gruner, U. Wiesner, The plumber's nightmare: A new morphology in block copolymer–ceramic nanocomposites and mesoporous aluminosilicates. *J. Am. Chem. Soc.* **125**, 13084–13093 (2003).
50. J. Ilavsky, *Nika*: Software for two-dimensional data reduction. *J. Appl. Crystallogr.* **45**, 324–328 (2012).
51. S. Brunauer, P. H. Emmett, E. Teller, Adsorption of gases in multimolecular layers. *J. Am. Chem. Soc.* **60**, 309–319 (1938).
52. E. P. Barrett, L. G. Joyner, P. P. Halenda, The determination of pore volume and area distributions in porous substances. I. Computations from nitrogen isotherms. *J. Am. Chem. Soc.* **73**, 373–380 (1951).

Acknowledgments: We thank R. T. Bell for advice and assistance with the fabrication of conductivity measurement substrates. **Funding:** H.S. was supported by the NSF Single Investigator Award (DMR-1104773). P.A.B. was supported by the NSF Graduate Research Fellowship Program (DGE-1144153). J.P.S. was supported by NSF DMR-1312160. This work was supported as part of the Energy Materials Center at Cornell (EMC2), an Energy Frontier Research Center funded by the U.S. Department of Energy, Office of Science, Basic Energy Sciences, under award DE-SC0001086. This work used the Cornell Center for Materials Research Shared Facilities, which were supported through the NSF Materials Research Science and Engineering Center program (DMR-1120296); the Cornell High Energy Synchrotron Source, which was supported by the NSF and the NIH/National Institute of General Medical Sciences under NSF award DMR-0936384; the Cornell NanoScale Facility, a member of the National Nanotechnology Coordinated Infrastructure (NNCI), which is supported by the NSF (Grant ECCS-15420819); and the x-ray detector laboratory of S.M.G., which was supported by U.S. Department of Energy grant DE-FG02-11ER16210. **Author contributions:** U.W. and S.M.G. conceived the idea and J.P.S. helped identify nitride as the material of interest. S.W.R., R.B.V., and U.W. came up with the experimental design. S.W.R. and P.A.B. synthesized the samples and performed the room-temperature conductivity, magnetization, and XRD measurements. P.A.B. performed the low-temperature conductivity and high-field magnetization measurements. S.W.R. performed the N_2 sorption measurements. H.S., P.A.B., and S.M.G. measured and analyzed the SAXS data. K.W.T. conducted the SEM characterization. J.G.W. conducted the TEM characterization. F.J.D. supervised and analyzed the XRD experiments. R.B.V. supervised and analyzed the magnetization and conductivity experiments. S.W.R., P.A.B., and U.W. wrote the paper with help from F.J.D., S.M.G., and J.P.S. All authors commented on the manuscript. U.W. supervised the project. **Competing interests:** The authors declare that they have no competing interests. **Data and materials availability:** All data needed to evaluate the conclusions in the paper are present in the paper and/or the Supplementary Materials. Additional data related to this paper may be requested from the authors.

Submitted 17 August 2015
Accepted 24 November 2015
Published 29 January 2016
10.1126/sciadv.1501119

Citation: S. W. Robbins, P. A. Beaucage, H. Sai, K. W. Tan, J. G. Werner, J. P. Sethna, F. J. DiSalvo, S. M. Gruner, R. B. Van Dover, U. Wiesner, Block copolymer self-assembly–directed synthesis of mesoporous gyroidal superconductors. *Sci. Adv.* **2**, e1501119 (2016).

ScienceAdvances
AAAS

Block copolymer self-assembly–directed synthesis of mesoporous gyroidal superconductors

Spencer W. Robbins, Peter A. Beaucage, Hiroaki Sai, Kwan Wee Tan, Jörg G. Werner, James P. Sethna, Francis J. DiSalvo, Sol M. Gruner, Robert B. Van Dover and Ulrich Wiesner (January 29, 2016)

Sci Adv 2016, 2:.
doi: 10.1126/sciadv.1501119